Open-Circuit Fault Tolerant Study of Bearingless Multi-Sector Permanent Magnet Machines

G. Valente[1]*, L. Papini[1,2]**, A. Formentini[1], C. Gerada[1,2], P. Zanchetta[1]
1 Electrical and Electronic Engineering, Univeristy of Nottingham, Nottingham, UK
2 Electrical and Electronic Engineering, Univeristy of Nottingham, Ningbo, China
*E-mail: ezzgv1@nottingham.ac.uk
**E-mail: ezzlp3@exmail.nottingham.ac.uk

***Abstract*—This paper presents a fault tolerant study of a multiphase sectored permanent magnet synchronous machine involving a tripel three-phase winding. The machine electromegnetic model is written in a general way so that it can be extended and applied to all machines with a similar winding structure. An expression of the $d-q$ axis reference currents of each three-phase winding as a function of the $x-y$ force components and torque is provided taking into acccunt the Joule losses minimization. Then, the case of open-circuit of one winding sector is considered, the model of the faulty machine derived and an expression of the new reference currents needed to generate radial suspension force and motoring torque is written.**
Finally, the theoretical analysis are validated through finite elements simulations and the levitation performance of the machine considered are evaluated in the Matlab-Simulink environment in the case of one sector fault per time.

***Index Terms*—Bearingless motor, Fault Tolerant, Force Control, Permanent Magnet Machines, Multiphase Motors.**

I. Introduction

The bearingless machines (BM), sometimes also referred as self-bearing machines, own the potential of producing motoring torque and radial suspension force simultaneously and with a single stator element. Therefore, they have the advantage of presenting no wear caused by friction, making them particularly suitable for lubricant free applications. As a matter of facts, they have found space in chemical, pharmaceutical and semiconductor industries where an ultra-high cleanness environment has to be guaranteed. More in the specific, the most targeted applications for BMs are centrifugal pumps [1], [2] and artificial hearts [3], [4], mixers for chemical and pharmaceutical applications [5], [6].

A primitive bearingless motor prototype was proposed by Hermann in the middle of 1970s [7]. Then only in the early 1990s the BM technology started attracting growing interest and it was first applied to reluctance motors [8] and then to induction motors [9] and permanent magnet synchronous motors [10]. The latter are of particular interest because of their advantage of simple structure, reliability, high efficiency and high torque density [11].

Typically, two separated windings were employed for torque and radial suspension force generation [8], [10]. The installation of the additional winding for force production leads to a bigger outer diameter than that of the conventional motor. Different winding arrangements has been presented in order to embed radial suspension force and torque generation in a single winding set. In [9] one of the phases of a four-pole induction motor was split into four so that each resultant coil could be supplied independently and used to control the radial rotor position. [12] exploited the concept of bridge configured winding where parallel branches were connected and the current through them could be controlled unbalancing the airgap magnetic field and generating a resultant force.

More recently, multiphase winding structures have been considered for their high power density, simple structure and fault tolerant capability. In particular, [13] presents a bearingless five-phase PM motor where the multiphase winding was exploited to control two decoupled $d-q$ planes for torque and radial force production, respectively. [14] the suspension force and motoring torque of a multi-three phase bearingless machine are controlled by means the Space Vector Decomposition (SVD) technique. In [15] a three three-phase sectored PMSM with a similar winding structure of the machine considered in this paper relied on the independent $d-$axis and $q-$axis current control of each winding to control suspension force and torque respectively. An harmonic compensator was then employed to suppress the force ripple caused by neglecting the coupling effect of torque and force production. The same authors have also tested the radial force technique for an open-circuit fault of one sector in [16] demonstrating the fault tolerant capability of the considered machine. A fault tolerant six-phase PM bearingless motor was proposed in [17] where each phase was controlled by a single phase inverter and an efficient reference current calculation was proposed. The multiphase structure and control method proposed allowed for fault tolerant operations when one or two phases were open-circuited.

The short-circuit fault instead was studied for a single-winding bearingless switched reluctance motor in [18] and for a six-phase bearingless PM motor in [19].

In this paper the open-circuit fault tolerant capabilities of the bearingless multi-sector PMSM are studied and a model for the faulty machine is carried out. The machine is a 18 slot - 6 poles PMSM with three three-phase windings [20], [21]. Open-circuit faults are considered involving the loss of a whole machine sector. It will be shown that the machine is still able to produce controllable torque and radial suspension force with two out of three healthy sectors. The torque and radial force

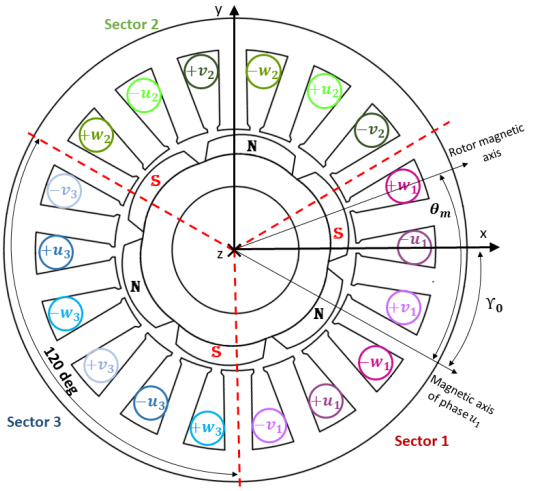

Fig. 1. Cross section of the 18 slot - 6 poles – 3 sectors PMSM with 3 × 3 single layer distributed winding.

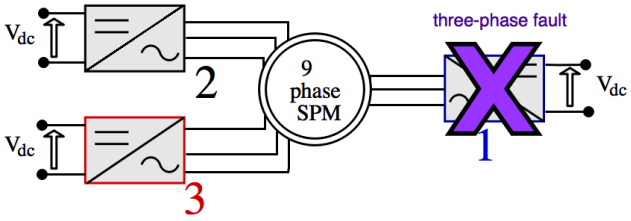

Fig. 2. MSPM machine connected to three three-phase inverters and open-circuit fault in inverter 1.

control technique employed in this work was presented in [20] and compared to the one applied to a similar machine in [15] showing advantages in terms of computational efforts. This work will also show that the control technique allows a simple formulation of the model for the faulty machine.

II. Mathematical model of the BMSPM machine

This section deals with the theoretical aspects of the radial suspension force and torque control for both healthy and fault operating conditions. At first the machine structure is presented and then the force production principles and the mathematical model for both operating conditions are exposed.

A. The machine structure

Fig. 1 displays the cross section of the machine considered highlighting its multi-three phase winding arrangement. The machine is a conventional surface mounted PM synchronous motor and its main features are listed in Table I. The original three-phase winding was removed and three full-pitched distributed star-connected windings with floating neutral points were installed. Each of the three windings occupies one third of the stator circumference and there is no overlapping between different sectors.

TABLE I
Machine Parameters

Parameter	Value
Pole number ($2p$)	6
PM material	NdFeB
Power rating	1.5 [kW]
Nominal current peak (I_n)	13 [A]
Rated Speed (ω_m^{max})	2π50 [rad/s]
PM flux of one sector (Λ_{PM})	0.0284 [Wb]
Torque constant (k_T)	0.128 [Nm/A]
Line to line voltage constant (k_V)	15.5 [V/krpm]
Rotor mass (m)	2 [Kg]
Magnetic stiffness (k_m)	0.7 [N/μm]
Backup bearing clearance (δ_{max})	150 [μm]
Outer Stator diameter	95 [mm]
Inner Stator diameter	49.5 [mm]
Axial length	90 [mm]
Airgap length	1 [mm]

B. Force production principles

Qualitatively, it can be observed that the airgap flux density distribution can be unbalanced controlling the current of each sector winding independently. In particular, assuming $\gamma_0 = 0$ (sector 1 aligned with the $x-$axis) in Fig. 1, a resultant net radial force in the $x-$ axis direction can be generated in healthy conditions increasing the flux density in the airgap underneath sector 1 and reducing the ones in correspondence of sector 2 and 3.
Fig. 2 shows a schematic representation of an open-circuit fault of the three-phase inverter connected to sector 1. Now, the remaining healthy sectors have to compensate the loss of sector 1 to the force production. Radial force can still be generated along the $x-$axis decreasing the flux density distribution in the airgap underneath sector 2 and 3. On the other hand, decreasing the flux density distribution in correspondence of sector 3 and increasing the one of sector 2 produces a force in the $y-$axis direction.

C. Healthy machine model

This paragraph provides the fundamental equations of the mathematical model for the healthy machine that was introduced and well detailed in [20]. The model is based on the assumptions of linear magnetic behaviour of the materials and magnetic decoupling between sectors. The latter allows to remarkably simplify the model since only one machine sector can be studied and the former permits to apply the superposition principle. Furthermore, the rotor is modelled as a rigid body that can move radially within a certain displacement δ_{max} given by the clearance of the backup bearing. The rotor radial displacement is defined by the translation δ and angle φ_d of the rotor centre from the rectangular $x-y$ reference frame origin of the stator O_s.
In this work, the number of machine sectors is $n_s = p$ and the angular position between the generic sector s and the x-axis is given by ${}^s\gamma = s\,(2\pi)/n_s + \gamma_0$. Under the aforementioned assumptions the matrix formulation of the $x-y$ force components and torque can be expressed in (1) as a function of the electrical angular position $\vartheta_e = p\vartheta_m$,

radial displacement information and stationary reference frame current components ${}^s i_\alpha$ and ${}^s i_\beta$ of each sector s.

$$\bar{W}_E = \mathbf{K}_E(\vartheta_e, {}^s\gamma)\bar{i}_{\alpha\beta} + \bar{K}_m(\varphi_d)\delta \tag{1}$$

Where $\bar{W}_E = \begin{bmatrix} F_x & F_y & T \end{bmatrix}^T$ and $\bar{i}_{\alpha\beta} = \begin{bmatrix} {}^1i_\alpha & {}^1i_\beta & \cdots & {}^si_\alpha & {}^si_\beta & \cdots & {}^{n_s}i_\alpha & {}^{n_s}i_\beta \end{bmatrix}^T$ are the mechanical $x-y$ forces and torque vector and the total vector of the $\alpha-\beta$ axis currents, respectively. The structure of matrix $\mathbf{K}_E(\vartheta_e, {}^s\gamma) \in \mathbb{R}^{3\times 2n_s}$ is reported in (2) showing the contributions of the n_s machine sectors to the force and torque production.

$$\mathbf{K}_E = \begin{bmatrix} {}^1\mathbf{K}_E(\vartheta_e, {}^1\gamma) \cdots {}^{n_s}\mathbf{K}_E(\vartheta_e, {}^{n_s}\gamma) \end{bmatrix} \tag{2}$$

The structure and the calculation procedure of sub-matrices ${}^1\mathbf{K}_E(\vartheta_e, {}^1\gamma), \ldots, {}^{n_s}\mathbf{K}_E(\vartheta_e, {}^1\gamma)$ is presented in [20], [22].
The reference current commands can be calculated inverting matrix $\mathbf{K}_E$. However, $\mathbf{K}_E$ results in general in a rectangular matrix, hence it cannot be easily inverted. In [20] the minimization of the copper losses has been chosen as strategy leading to the calculation of the pseudo inverse of $\mathbf{K}_E$ as follow

$$\mathbf{K}_E^+ = \mathbf{K}_E^T(\mathbf{K}_E\mathbf{K}_E^T)^{-1} \tag{3}$$

Therefore, the current command vector $\bar{i}^*_{\alpha\beta}$ can be determined in (4) considering also the rotor displacement.

$$\bar{i}^*_{\alpha\beta} = \mathbf{K}_E^+\left[\bar{W}_E^* - \bar{K}_m(\varphi_d)\delta\right] = \mathbf{K}_E^+\left[(\bar{W}_E^* - k_m \begin{bmatrix} u \\ v \\ 0 \end{bmatrix}\right] \tag{4}$$

Where u and v are the $x-$ and $y-$ axis displacements and k_m is the magnetic radial stiffness [22].
Conventional PI controllers require $d-q$ axis current in the rotor synchronous reference frame. Hence, $\bar{i}^*_{\alpha\beta}$ has to be multiplied by a rotating matrix as in (5) to obtain the reference currents in the $d-q$ reference frame.

$$\bar{i}^*_{dq} = \mathbf{T}_{R9}(\vartheta_e)\bar{i}^*_{\alpha\beta} = \mathbf{K}^+_{E,dq}\left[\bar{W}_E^* - \bar{K}_m(\varphi_d)\delta\right] \tag{5}$$

Where $\mathbf{T}_{R9}(\vartheta_e)$ is the nine-phase rotation matrix and $\mathbf{K}^+_{E,dq}$ is the pseudo inverse matrix in the rotor synchronous reference frame. The latter can be found in the Appendix .

D. Open circuit fault condition

When an open-circuit fault occurs in one motor sector the correspondent $d-q$ axis current vector goes to zero eliminating its contribution to the radial force and torque production. Therefore, the sub-matrix related to the open-circuited sector will disappear in $\mathbf{K}_E$ and the new matrices expressions can be written as

$$\begin{aligned} \mathbf{K}_{E,f1} &= \begin{bmatrix} {}^2\mathbf{K}_E(\vartheta_e, {}^2\gamma) & {}^3\mathbf{K}_E(\vartheta_e, {}^3\gamma) \end{bmatrix} \\ \mathbf{K}_{E,f2} &= \begin{bmatrix} {}^1\mathbf{K}_E(\vartheta_e, {}^1\gamma) & {}^3\mathbf{K}_E(\vartheta_e, {}^3\gamma) \end{bmatrix} \\ \mathbf{K}_{E,f3} &= \begin{bmatrix} {}^1\mathbf{K}_E(\vartheta_e, {}^1\gamma) & {}^2\mathbf{K}_E(\vartheta_e, {}^2\gamma) \end{bmatrix} \end{aligned} \tag{6}$$

for open-circuit in sector 1, 2, 3, respectively. It can be noticed that matrices $\mathbf{K}_{E,f1}$, $\mathbf{K}_{E,f2}$ and $\mathbf{K}_{E,f3} \in \mathbb{R}^{3\times(2n_s-2)}$ are also rectangular. Therefore, in order to obtain the reference current signals in the case of open-circuit fault conditions, they can be substituted into (3) obtaining $\mathbf{K}^+_{E,f1}$, $\mathbf{K}^+_{E,f2}$ and $\mathbf{K}^+_{E,f3} \in \mathbb{R}^{(2n_s-2)\times 3}$ respectively that in turn can be used in place of $\mathbf{K}_E^+$ in (4) to calculate the $\alpha-\beta$ reference current vectors. The $d-q$ reference current values are then calculated as follow

$$\begin{aligned} \bar{i}^*_{dq,f1} &= \hat{\mathbf{K}}^+_{E,f1}\left[\bar{W}_E^* - \bar{K}_m(\phi_d)\delta\right] \\ \bar{i}^*_{dq,f2} &= \hat{\mathbf{K}}^+_{E,f2}\left[\bar{W}_E^* - \bar{K}_m(\phi_d)\delta\right] \\ \bar{i}^*_{dq,f3} &= \hat{\mathbf{K}}^+_{E,f3}\left[\bar{W}_E^* - \bar{K}_m(\phi_d)\delta\right] \end{aligned} \tag{7}$$

$\hat{\mathbf{K}}^+_{E,f1}$, $\hat{\mathbf{K}}^+_{E,f2}$ and $\hat{\mathbf{K}}^+_{E,f3}$ are the pseudo inverse matrices in the rotor reference frame in the case of fault in sector 1, 2 and 3 respectively. Their expressions are reported in the Appendix. $\bar{i}^*_{dq,oc1} = \begin{bmatrix} {}^2i_d & {}^2i_q & {}^3i_d & {}^3i_q \end{bmatrix}^T$, $\bar{i}^*_{dq,oc2} = \begin{bmatrix} {}^1i_d & {}^1i_q & {}^3i_d & {}^3i_q \end{bmatrix}^T$ and $\bar{i}^*_{dq,oc3} = \begin{bmatrix} {}^1i_d & {}^1i_q & {}^2i_d & {}^2i_q \end{bmatrix}^T$. On the other hand, ${}^1\bar{i}^*_{dq,oc1} = \begin{bmatrix} 0 & 0 \end{bmatrix}^T$, ${}^2\bar{i}^*_{dq,oc2} = \begin{bmatrix} 0 & 0 \end{bmatrix}^T$ and ${}^3\bar{i}^*_{dq,oc3} = \begin{bmatrix} 0 & 0 \end{bmatrix}^T$ when the open circuit fault occurs in sector 1,2 and 3, respectively.
Fig. 3 shows the harmonic content of the coefficients of matrix $\mathbf{K}_E^+ \in \mathbb{R}^{6\times 3}$, for healthy operating condition and of matrices $\mathbf{K}_{E,f1}$, $\mathbf{K}_{E,f2}$ and $\mathbf{K}_{E,f3} \in \mathbb{R}^{4\times 3}$ for an open-circuit fault in sector 1, 2 and 3, respectively. The magnitudes of the harmonics have been obtained through the fast Fourier transform of the aforementioned coefficients waveforms presented in [20]. It can be noticed that the first two lines do not contain the coefficients of matrix $\mathbf{K}_{E,f1}$ since the current components of sector 1 are null in the case of open-circuit fault. The same is true for matrices $\mathbf{K}_{E,f2}$ and $\mathbf{K}_{E,f3}$. Their coefficients do not appear in lines 3, 4 and lines 5, 6, respectively. Comparing the different harmonic contents it can be observed that a non negligible third harmonic appears in the terms of matrices $\mathbf{K}_{E,f1}$, $\mathbf{K}_{E,f2}$ and $\mathbf{K}_{E,f3}$, while the ones of $\mathbf{K}_E$ are essentially sinusoidal. Their waveforms were reported in [20] and they can be easily implemented in a DSP reducing the computational efforts. On the other hand, the third harmonic has to be considered in the coefficients of $\mathbf{K}_{E,f1}$, $\mathbf{K}_{E,f2}$ and $\mathbf{K}_{E,f3}$ in order to produce the required suspension force and motoring torque complicating the control algorithm.

III. Finite Elements Simulation Results

In this section the FE validation of the mathematical model written for open-circuit fault is presented. The FE software employed is MagNet 7.7.1. Fig. 4, 5 and 6 a)-b) show the force production for healthy and open-circuit fault in sector 1, 2 and 3 respectively considering two case studies: a) setting $T_E^* = 0$; b) setting $T_E^* = 2.7[Nm]$.
In the simulations the rotor is rotated of two whole mechanical revolutions (720 deg) while the force reference magnitude

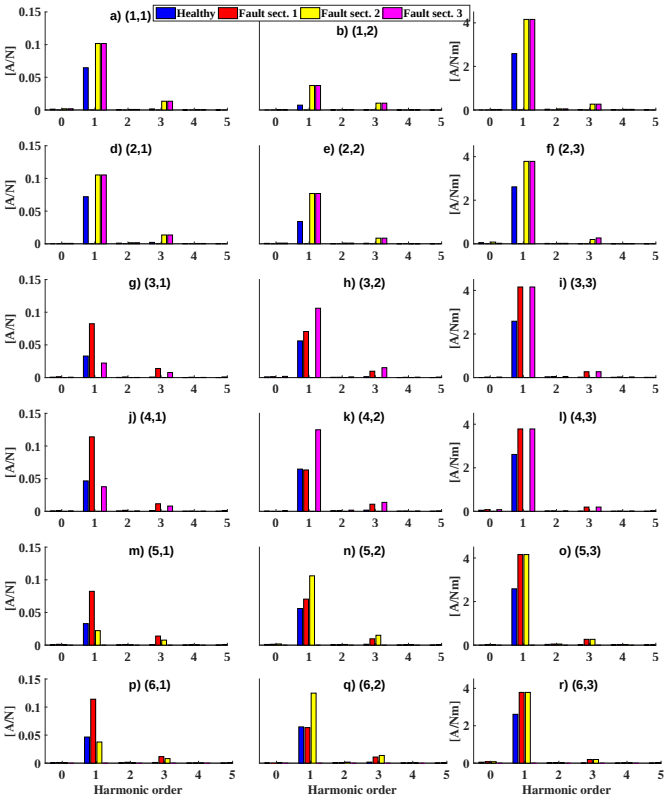

Fig. 3. Comparison in terms of harmonic content between the coefficients of matrix $\mathbf{K}_E^+$ (healthy machine), matrix $\mathbf{K}_{E,f1}^+$ (fault in sector 1), matrix $\mathbf{K}_{E,f2}^+$ (fault in sector 2) and matrix $\mathbf{K}_{E,f3}^+$ (fault in sector 3). (r, c) stands for the coefficient in the r^{th} row and c^{th} column.

$|F_E|^*$ is kept constant and the direction $\angle F_E^*$ varies from 0 to 360 deg with steps of 120 deg as it is possible to observe in the figures. In order to satisfy the current limit of the machine the force reference magnitude $|F_E|^* = 100$ N is halved when torque is also produced.

It is possible to observe from Fig. 4, 5 and 6 a) that the force ripple remains about the same when a fault occurs and no torque is produced. On the other hand, when torque is simultaneously generated the ripple slightly increases as depicted in Fig. 4, 5 and 6 b). The above observations can be quantified in terms of Total Harmonic Distortion (THD) of the $x-y$ axis force components and summarized in Table II for all the considered case studies. It is straightforward to see that the highest THD occurs for an open-circuit fault in sector 3 for $T_E = 2.7$ N. The THD obtained is 7.42 % which is only 3 % higher than the one obtained at no-load.

Finally, the torque generated during healthy and faulty conditions can be examined in Fig. 4, 5 and 6 c) showing that the torque ripple is not significantly affected by the open-circuit faults.

IV. Numerical Simulation Results

A. Simulation structure

Fig. 7 shows the block scheme of the simulation implemented in the Simulink-Matlab environment. It is possible to

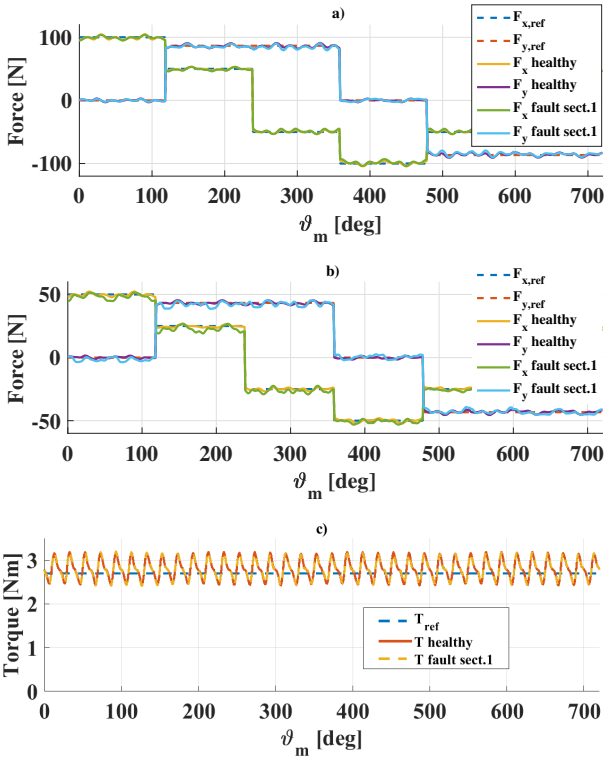

Fig. 4. Force and torque generation with open-circuit fault in sector 1: a) $x-y$ axis force production for $T_{ref} = 0$; b) $x-y$ axis force production for $T_{ref} = 2.7[Nm]$; c) torque production setting $T_{ref} = 2.7[Nm]$.

distinguish three different regions: the control algorithm (in green) operating in the discrete domain at the sample time $T_s = 100$ $[\mu s]$; the electro-mechanical model of the MSPM motor (in yellow) simulated in the continuous domain; the rotor-dynamic model of the rotor (in red) implemented in discrete with $T_{ss} = 1$ $[\mu s]$.

The control algorithm includes the position and speed controllers, responsible for the suspension force and torque references calculation, the mathematical model described in (4), (5) for healthy machine and in (6), (7) for faulty machine and the blocks delay z^{-2} representing the current controllers. As a matter of fact, a well tuned current controller introduces a delay of two sample times T_s between the reference current and motor current (if no voltage saturation occurs). The design of the position controller considered in this work can be found in [23]. The speed loop controller is a standard PI controller as the one proposed in [24]. The electro-mechanical model of the motor considered is stored in the form of lookup table and it maps the $d-q$ axis currents to $x-y$ force components and torque. The lookup table has been carried out by means "multi-static" non-linear FE simulations to take into account the iron saturation. The rotor weight force and an eventual disturbance are then added and the resultant $F_{x,t}$ and $F_{y,t}$ forces are the input of the rotor dynamic model block represented by

$$\begin{bmatrix} m & 0 \\ 0 & m \end{bmatrix} \begin{bmatrix} \ddot{u} \\ \ddot{v} \end{bmatrix} - \begin{bmatrix} k_m & 0 \\ 0 & k_m \end{bmatrix} \begin{bmatrix} u \\ v \end{bmatrix} = \begin{bmatrix} F_{x,c} + F_{x,d} \\ F_{y,c} + F_{y,d} - mg \end{bmatrix} \quad (8)$$

TABLE II
THD OF THE FORCE GENERATION

	$T_E = 0Nm$				$T_E = 2.7Nm$			
	Healthy	Fault 1	Fault 2	Fault 3	Healthy	Fault 1	Fault 2	Fault 3
F_x	4.31	5.1	4.58	4.56	4.05	7.22	6.64	7.42
F_y	3.56	3.77	4.04	4.02	3.25	5.27	5.52	5.11

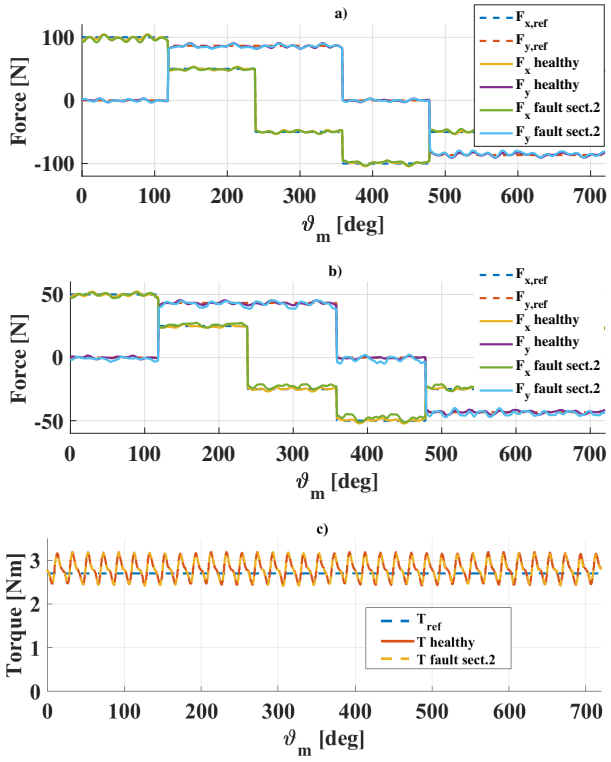

Fig. 5. Force and torque generation with open-circuit fault in sector 2: a) $x-y$ axis force production for $T_{ref} = 0$; b) $x-y$ axis force production for $T_{ref} = 2.7[Nm]$; c) torque production setting $T_{ref} = 2.7[Nm]$.

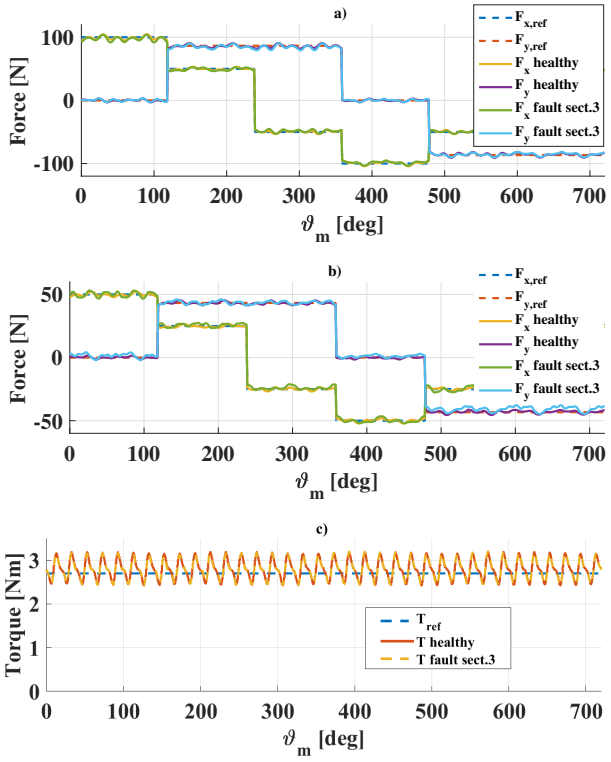

Fig. 6. Force and torque generation with open-circuit fault in sector 3: a) $x-y$ axis force production for $T_{ref} = 0$; b) $x-y$ axis force production for $T_{ref} = 2.7[Nm]$; c) torque production setting $T_{ref} = 2.7[Nm]$.

where u and v are the rotor $x-y$ axis displacements and $F_{x,c}$, $F_{y,c}$ and $F_{x,d}$, $F_{y,d}$ are the $x-y$ components of the forces generated by the controller and by the disturbance, respectively.

The simulation also presents a fault selector block that allows to easily simulate a fault, hence setting the currents of the faulty sector to zero and switching from healthy to faulty mathematical models.

B. Simulation results

The results of the simulation for open-circuit faults are displayed in Fig. 8, 9 and 10. A simulation time of 1 s is considered.

At first, the fault selector is set to 0 and the rotor is positioned in the stator centre after an initial short transient (Fig. 8 a)). Then at 0.02 and 0.04 s the rotor speed is commanded to its rated value (Fig. 9 a)) and force disturbance is applied in the $y-$ axis (Fig. 8 b)) respectively justifying the first perturbation in the rotor position observed in Fig. 8 a) and the increase of the $d-q$ axis currents in the motor sectors observed in Fig. 10 a)-c). The aforementioned force disturbance $F_{y,d} = -100$ N has a duration of 0.02 s. At 0.1 s, then, the load torque is set equal to 3 Nm (Fig. 9 b)) justifying the increment of the $q-$axis currents of the three sectors (Fig. 10).

While the simulation is running the fault selector is manually set to 1 in order to simulate a sudden open-circuit fault in sector 1. It can be observed from Fig. 8 a) that the position controller achieves to maintain the rotor centred after a very small position transient. Fig. 10 a) shows that, for the duration of the fault, the $d-q$ currents of sector 1 is zero while Fig. 10 b) and c) show that the ones of sectors 2 and 3 increase their magnitudes to compensate the loss of the contribution of sector 1 to the force generation. From Fig. 10 b) and c) it can also be noticed that the current ripple of the healthy sectors is remarkably increased after the fault occurs. This phenomena could be predicted observing the increment of the current distortion depicted in Fig. 3. The previously described force disturbance is applied during the fault (Fig. 8 b)) in order to verify the disturbance rejection capability of the faulty bearingless drive.

The same procedure is followed to simulate the open-circuit fault in sectors 2 and 3 showing a similar behaviour.

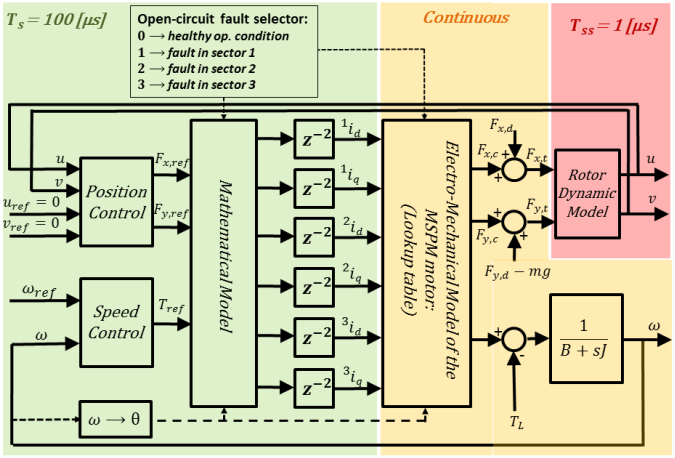

Fig. 7. Block scheme implemented in the MATLAB-Simulink environment.

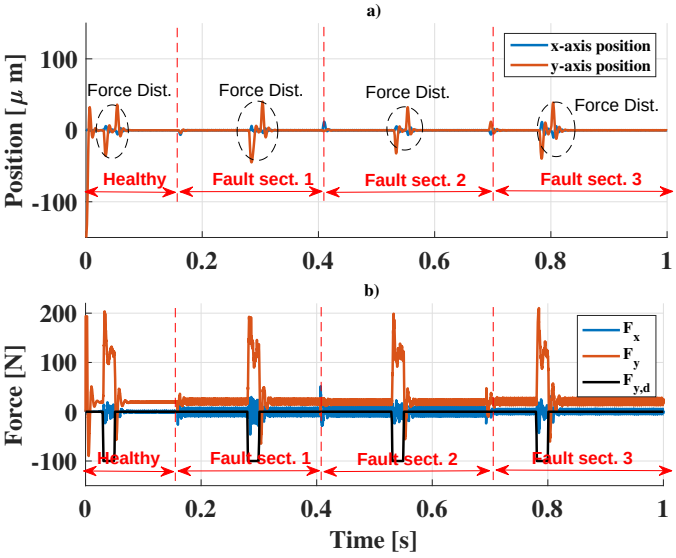

Fig. 8. Result of the numerical simulation for bearingless operation in open-circuit fault condition: a) $x-y$ axis rotor position; b) $x-y$ axis generated forces and $y-$axis force disturb.

V. Conclusions

A 6-pole PMSM featuring multi-sector multi-phase winding arrangement has been considered. The machine has been analysed for healthy and open-circuit fault conditions providing a detailed mathematical model for the electromagnetic torque and radial force production. FE simulation results for radial suspension force and motoring torque production are provided. The levitation performance for healthy and faulty machine are studied by means numerical simulations performed in the Simulink-Matlab environment showing good fault capability of the bearingless drive.

Appendix

A. Healthy operating condition

The pseudo inverse matrix in the rotor synchronous reference frame was introduced in (5). It can be explicated as

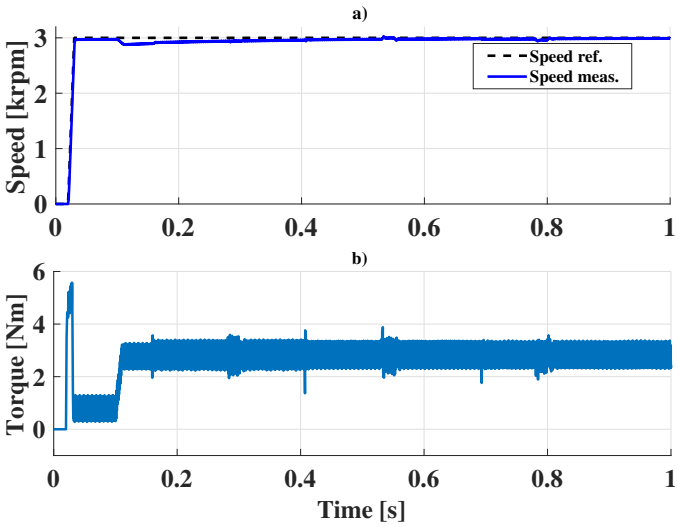

Fig. 9. Result of the numerical simulation for bearingless operation in open-circuit fault condition: a)rotor speed; b) generated torque.

follow

$$\mathbf{K}^{+}_{E,dq}(\vartheta_e) = \begin{bmatrix} {}^{1}k^{+}_{xd}(\vartheta_e) & {}^{1}k^{+}_{yd}(\vartheta_e) & 0 \\ {}^{1}k^{+}_{xq}(\vartheta_e) & {}^{1}k^{+}_{yq}(\vartheta_e) & -k'_T \\ {}^{2}k^{+}_{xd}(\vartheta_e) & {}^{2}k^{+}_{yd}(\vartheta_e) & 0 \\ {}^{2}k^{+}_{xq}(\vartheta_e) & {}^{2}k^{+}_{yq}(\vartheta_e) & -k'_T \\ {}^{3}k^{+}_{xd}(\vartheta_e) & {}^{3}k^{+}_{yd}(\vartheta_e) & 0 \\ {}^{3}k^{+}_{xq}(\vartheta_e) & {}^{3}k^{+}_{yq}(\vartheta_e) & -k'_T \end{bmatrix} \tag{9}$$

where $k'_T = 1/3k_T$ [A/Nm] and the expression of the generic coefficient ${}^{s}k^{+}_{*\times}(\vartheta_e)$ is

$${}^{s}k^{+}_{*\times}(\vartheta_e) = {}^{s}c_{*\times} + {}^{s}s_{*\times}\cos(2\vartheta_e + {}^{s}\varphi_{*\times}) \tag{10}$$

It is possible to notice that ${}^{s}k^{+}_{*\times}(\vartheta_e)$ presents a constant and a sinusoidal term. The latter pulsates at twice the electrical frequency and produces a non-constant $d-q$ axis current reference signals.
The angle γ_0 is required for the calculation of parameters ${}^{s}c_{*\times}$, ${}^{s}s_{*\times}$ and ${}^{s}\varphi_{*\times}$. As a matter of facts, γ_0 was defined in Section II as the angular position of the magnetic axis of the sector 1 with respect to the $x-$axis. As an example, Table III reports the above mentioned parameters calculated for $\gamma_0 = 0$.

B. Open-circuit operating condition

In order to describe the model in the rotor synchronous reference frame, matrices $\mathbf{K}^{+}_{E,f1}$, $\mathbf{K}^{+}_{E,f2}$ and $\mathbf{K}^{+}_{E,f3}$ have to be replaced with $\hat{\mathbf{K}}^{+}_{E,f1}$, $\hat{\mathbf{K}}^{+}_{E,f2}$ and $\hat{\mathbf{K}}^{+}_{E,f3}$ obtained as follow:

$$\begin{aligned} \hat{\mathbf{K}}^{+}_{E,f1}(\vartheta_e) &= \mathbf{T}_{R,f}(\vartheta_e)\mathbf{K}^{+}_{E,f1}(\vartheta_e) \\ \hat{\mathbf{K}}^{+}_{E,f2}(\vartheta_e) &= \mathbf{T}_{R,f}(\vartheta_e)\mathbf{K}^{+}_{E,f2}(\vartheta_e) \\ \hat{\mathbf{K}}^{+}_{E,f3}(\vartheta_e) &= \mathbf{T}_{R,f}(\vartheta_e)\mathbf{K}^{+}_{E,f3}(\vartheta_e) \end{aligned} \tag{11}$$

where $\mathbf{T}_{R,f}$ is the six-phase rotation matrix.
The expressions of the force and torque coefficients contained

TABLE III
PARAMETERS OF FORCE COEFFICIENTS

	Sector 1				Sector 2				Sector 3			
	x,d	x,q	y,d	y,q	x,d	x,q	y,d	y,q	x,d	x,q	y,d	y,q
${}^{s}c_{*\times}$ [A/N]	0.068	0	0	0.021	0.034	0.018	0.058	0.01	0.034	0.018	0.058	0.01
${}^{s}s_{*\times}$ [A/N]	0.0055	0.0025	0.014	0.013	0.012	0.0112	0.0083	0.0068	0.0121	0.0121	0.0083	0.0068
${}^{s}\varphi_{*\times}$ [rad]	0.0622	1.63	1.63	-3.08	-1.74	-0.05	-0.9	0.39	1.86	-2.97	-2.12	-0.26

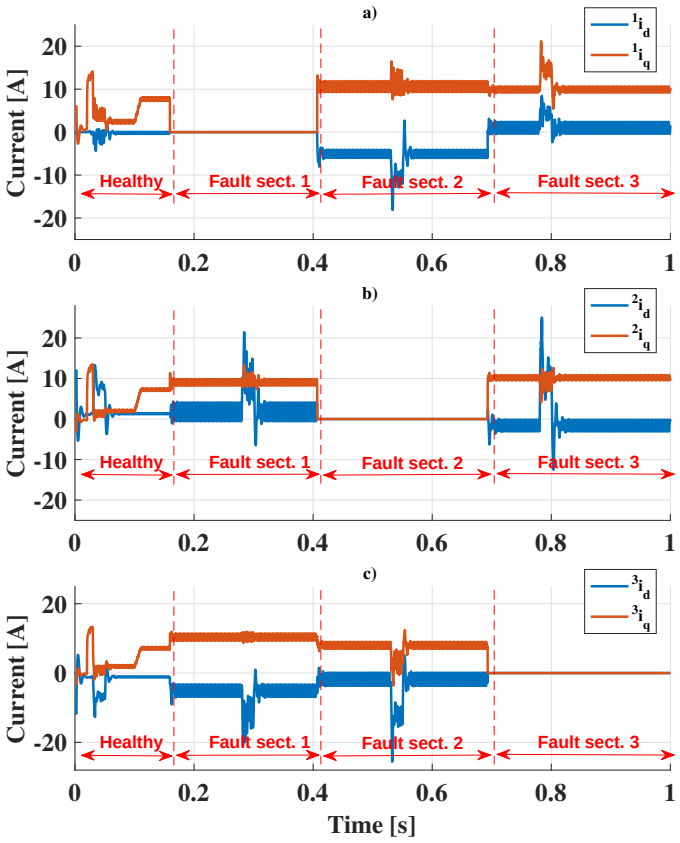

Fig. 10. Result of the numerical simulation for bearingless operation in open-circuit fault condition: :a) $d-q$ axis currents sect. 1; b) $d-q$ axis currents sect. 2; c) $d-q$ axis currents sect. 3.

in the pseudo inverse matrix $\hat{\mathbf{K}}^{+}_{E,fs}$ related to the fault in a generic sector s can be found in (12) and (13), respectively.

$$
\begin{aligned}
{}^{s}k^{+}_{*\times,fs}(\vartheta_e) = {}^{s}c_{*\times,fs} + {}^{s}s_{*\times,fs}\cos(2\vartheta_e + {}^{s}\varphi_{*\times,fs}) + \\
+ {}^{s}r_{*\times,fs}\cos(4\vartheta_e + {}^{s}\psi_{*\times,fs})
\end{aligned}
\tag{12}
$$

$$
\begin{aligned}
{}^{s}k^{+}_{T\times,fs}(\vartheta_e) = {}^{s}c_{T\times,fs} + {}^{s}s_{T\times,fs}\cos(2\vartheta_e + {}^{s}\varphi_{T\times,fs}) + \\
+ {}^{s}r_{T\times,fs}\cos(4\vartheta_e + {}^{s}\psi_{T\times,fs})
\end{aligned}
\tag{13}
$$

It can be noticed that the coefficients of $\hat{\mathbf{K}}^{+}_{E,fs}$ still contain the second harmonic as in (10). Furthermore, a forth harmonic term appears due to the presence of the third harmonic in the coefficients of $\mathbf{K}^{+}_{E,fs}$ (see Fig. 3).

The parameters in (12) and (13) can be easily calculated once γ_0 is defined. As an example, the parameters of the force and torque coefficients for fault in sector 1 (matrix $\hat{\mathbf{K}}^{+}_{E,f1}$) have been calculated for $\gamma_0 = 0$ and they have been reported in Tables IV and V.

REFERENCES

[1] J. Asama, D. Kanehara, T. Oiwa, and A. Chiba, "Development of a compact centrifugal pump with a two-axis actively positioned consequent-pole bearingless motor," *IEEE Transactions on Industry Applications*, vol. 50, no. 1, pp. 288–295, Jan 2014.

[2] K. Raggl, B. Warberger, T. Nussbaumer, S. Burger, and J. W. Kolar, "Robust angle-sensorless control of a pmsm bearingless pump," *IEEE Transactions on Industrial Electronics*, vol. 56, no. 6, pp. 2076–2085, June 2009.

[3] J. Asama, T. Fukao, A. Chiba, A. Rahman, and T. Oiwa, "A design consideration of a novel bearingless disk motor for artificial hearts," in *2009 IEEE Energy Conversion Congress and Exposition*, Sept 2009, pp. 1693–1699.

[4] Y. Okada, N. Yamashiro, K. Ohmori, T. Masuzawa, T. Yamane, Y. Konishi, and S. Ueno, "Mixed flow artificial heart pump with axial self-bearing motor," *IEEE/ASME Transactions on Mechatronics*, vol. 10, no. 6, pp. 658–665, Dec 2005.

[5] T. Reichert, T. Nussbaumer, and J. W. Kolar, "Bearingless 300-w pmsm for bioreactor mixing," *IEEE Transactions on Industrial Electronics*, vol. 59, no. 3, pp. 1376–1388, March 2012.

[6] B. Warberger, R. Kaelin, T. Nussbaumer, and J. W. Kolar, "50-nm/2500-w bearingless motor for high-purity pharmaceutical mixing," *IEEE Transactions on Industrial Electronics*, vol. 59, no. 5, pp. 2236–2247, May 2012.

[7] P. Hermann, "A radial active magnetic bearing," *London Patent*, no. 1, p. 478, 1973.

[8] A. Chiba, M. A. Rahman, and T. Fukao, "Radial force in a bearingless reluctance motor," *IEEE Transactions on Magnetics*, vol. 27, no. 2, pp. 786–790, March 1991.

[9] A. O. Salazar and R. M. Stephan, "A bearingless method for induction machines," *IEEE Transactions on Magnetics*, vol. 29, no. 6, pp. 2965–2967, Nov 1993.

[10] M. Oshima, S. Miyazawa, T. Deido, A. Chiba, F. Nakamura, and T. Fukao, "Characteristics of a permanent magnet type bearingless motor," *IEEE Transactions on Industry Applications*, vol. 32, no. 2, pp. 363–370, Mar 1996.

[11] G. Feng, C. Lai, and N. C. Kar, "An analytical solution to optimal stator current design for pmsm torque ripple minimization with minimal machine losses," *IEEE Transactions on Industrial Electronics*, vol. 64, no. 10, pp. 7655–7665, Oct 2017.

[12] W. K. S. Khoo, "Bridge configured winding for polyphase self-bearing machines," *IEEE Transactions on Magnetics*, vol. 41, no. 4, pp. 1289–1295, April 2005.

[13] J. Huang, B. Li, H. Jiang, and M. Kang, "Analysis and control of multiphase permanent-magnet bearingless motor with a single set of half-coiled winding," *IEEE Transactions on Industrial Electronics*, vol. 61, no. 7, pp. 3137–3145, July 2014.

[14] G. Sala, G. Valente, A. Formentini, L. Papini, D. Gerada, P. Zanchetta, A. Tani, and C. Gerada, "Space vectors and pseudo inverse matrix methods for the radial force control in bearingless multi-sector permanent magnet machines," *IEEE Transactions on Industrial Electronics*, vol. PP, no. 99, pp. 1–1, 2018.

TABLE IV
PARAMETERS OF FORCE COEFFICIENTS FOR FAULT IN SECT. 1

	Sector 1				Sector 2				Sector 3			
	x,d	x,q	y,d	y,q	x,d	x,q	y,d	y,q	x,d	x,q	y,d	y,q
${}^{s}c_{*\times,f1}$[A/N]	/	/	/	/	0.088	0.0427	0.0661	0	0.088	0.0427	0.0661	0
${}^{s}s_{*\times,f1}$[A/N]	/	/	/	/	0.0234	0.0204	0.0205	0.0039	0.0234	0.0204	0.0205	0.0039
${}^{s}r_{*\times,f1}$[A/N]	/	/	/	/	0.0018	0.003	0.0015	0.0016	0.0018	0.003	0.0015	0.0016
${}^{s}\varphi_{*\times,f1}$[deg]	/	/	/	/	-2.7	0.062	-1.63	-1.51	2.83	-3.1	-1.38	1.63
${}^{s}\psi_{*\times,f1}$[deg]	/	/	/	/	2.16	-3.02	2.55	-1.45	-1.91	0.12	0.84	1.7

TABLE V
PARAMETERS OF TORQUE COEFFICIENTS FOR FAULT IN SECT. 1

	Sector 1		Sector 2		Sector 3	
	T,d	T,q	T,d	T,q	T,d	T,q
${}^{s}c_{T\times,f1}$[A/N]	/	/	0.627	3.55	0.627	3.55
${}^{s}s_{T\times,f1}$[A/N]	/	/	0.523	0.0915	0.523	0.0915
${}^{s}r_{T\times,f1}$[A/N]	/	/	0.0442	0.0373	0.0442	0.0373
${}^{s}\varphi_{T\times,f1}$[deg]	/	/	-2.5	-1.51	-0.52	1.63
${}^{s}\psi_{T\times,f1}$[deg]	/	/	-1.93	-1.45	-0.96	1.7

[15] S. Kobayashi, M. Ooshima, and M. N. Uddin, "A radial position control method of bearingless motor based on d - q- axis current control," *IEEE Transactions on Industry Applications*, vol. 49, no. 4, pp. 1827–1835, July 2013.

[16] M. Ooshima, A. Kobayashi, and T. Narita, "Stabilized suspension control strategy at failure of a motor section in a d-q axis current control bearingless motor," in *2015 IEEE Industry Applications Society Annual Meeting*, Oct 2015, pp. 1–7.

[17] X. L. Wang, Q. C. Zhong, Z. Q. Deng, and S. Z. Yue, "Current-controlled multiphase slice permanent magnetic bearingless motors with open-circuited phases: Fault-tolerant controllability and its verification," *IEEE Transactions on Industrial Electronics*, vol. 59, no. 5, pp. 2059–2072, 2012.

[18] X. Cao, H. Yang, L. Zhang, and Z. Deng, "Compensation strategy of levitation forces for single-winding bearingless switched reluctance motor with one winding total short circuited," *IEEE Transactions on Industrial Electronics*, vol. 63, no. 9, pp. 5534–5546, Sept 2016.

[19] X. Wang, X. Ren, and J. Y. Zhang, "Short-circuit fault-tolerant control of bearingless permanent magnet slice machine," in *2013 IEEE Energy Conversion Congress and Exposition*, Sept 2013, pp. 1148–1153.

[20] G. Valente, L. Papini, A. Formentini, C. Gerada, and P. Zanchetta, "Radial force control of multi-sector permanent magnet machines," in *2016 XXII International Conference on Electrical Machines (ICEM)*, Sept 2016, pp. 2595–2601.

[21] ——, "Radial force control of multi-sector permanent magnet machines for vibration suppression," *IEEE Transactions on Industrial Electronics*, vol. PP, no. 99, pp. 1–1, 2017.

[22] ——, "Radial force control of multi-sector permanent magnet machines considering radial rotor displacement," in *2017 IEEE Workshop on Electrical Machines Design, Control and Diagnosis (WEMDCD)*, April 2017, pp. 140–145.

[23] G. Valente, A. Formentini, L. Papini, P. Zanchetta, and C. Gerada, "Position control study of a bearingless multi-sector permanent magnet machine," in *IECON 2017 - 43rd Annual Conference of the IEEE Industrial Electronics Society*, Oct 2017, pp. 8808–8813.

[24] M. Calvini, A. Formentini, G. Maragliano, and M. Marchesoni, "Self-commissioning of direct drive systems," in *Power Electronics, Electrical Drives, Automation and Motion (SPEEDAM), 2012 International Symposium on*. IEEE, 2012, pp. 1348–1353.